Optical Engineering

OpticalEngineering.SPIEDigitalLibrary.org

Recognition of interior photoelectric devices by using dual criteria of shape and local texture

Feng Qian
Bao Zhang
Chuanli Yin
Mingyu Yang
Xiantao Li

SPIE.

Recognition of interior photoelectric devices by using dual criteria of shape and local texture

Feng Qian,[a,b,c] Bao Zhang,[b,*] Chuanli Yin,[b] Mingyu Yang,[b,c] and Xiantao Li[b,c]
[a]The University of the Chinese Academy of Sciences, Yuquan Road 19A, Beijing 100049, China
[b]Chinese Academy of Sciences, Changchun Institute of Optics, Fine Mechanics and Physics, Department of Airborne Optical Imaging and Measurement, Dongnanhu Road 3888, Changchun, Jilin 130033, China
[c]Chinese Academy of Sciences, Key Laboratory of Airborne Optical Imaging and Measurement, Dongnanhu Road 3888, Changchun, Jilin 130033, China

Abstract. A necessity exists for the protection of people and their property against the unauthorized use of photoelectric devices. The retroreflection of optical systems can be utilized to detect and recognize photoelectric devices. The reduction of false alarms and processing speed are two crucial issues, particularly for interior applications involving complex scenes. Here, we propose a local texture criterion that determines the local maximum and local continuity of the reflections. A comprehensive evaluation method that combines a modified shape criterion and the local texture criterion to improve the recognition probability is also presented. A searching strategy for scanning and locating the target candidates with reduced time cost was used in laboratory experiments performed at operating distances of 2.2, 3.2, and 4.2 m with the presence of disturbing objects. The results demonstrated the practicability of the proposed method, its superior recognition probability over that of single-criterion methods, and its enhanced average processing speed in comparison with existing methods.
 [DOI: 10.1117/1.OE.54.12.123110]

Keywords: retroreflection recognition; cat's eye effect; local texture criterion; shape criterion; false alarm reduction.

Paper 151102 received Aug. 11, 2015; accepted for publication Nov. 23, 2015; published online Dec. 21, 2015.

1 Introduction

The detection and recognition of the interior photoelectric devices, such as miniature cameras, are significant for the protection of policy, commercial, technical, and private information. Examples include political events, commercial summits, drama theaters, trade shows, research laboratories, technical facilities, private rooms, and hotel rooms. The existing detecting systems addressing these problems are based on the retroreflection, or cat's eye effect, of the optical systems. Photoelectric devices are discriminated against spurious background by the stronger retroreflected signals emitted from the illumination subsystem of the detecting system and reflected by their own optical systems.

The methods reported in the literature have been mostly developed for open-terrain applications such as detecting sniper scopes. Lecocq et al.[1] proposed an image subtraction scheme for suppressing background clutter. Ren and Li[2] used dual criteria related to the shape of the retroreflection spot and the modulation frequency of the optical target. Li et al.[3] investigated the feasibility of using compressive sensing methods to remove dynamic backgrounds and to extract the target features. More systems have been proposed recently[4–8] with improved sensor techniques that acquire the features of spectral or chromatic effects and provide high-resolution range profiling of the optical targets. A multisensor-configuration fusion scheme has also been evaluated in Refs. 9 and 10.

However, the environmental qualities of interior applications are different from those of the open-terrain ones. Interior scenes contain much more interference. A system for detecting pirating video equipment in movie theaters is described in Ref. 11. The system was designed to prevent the unauthorized use of cameras by comparing the reflections of the on-axis and off-axis illumination. It has been observed that the retroreflection of optical devices appears in the image as a local maximum, e.g., a well-defined peak of bright pixels surrounded by dark pixels; whereas other false positives usually have some degree of continuity between the peak and its surroundings. However, no appropriate criterion has been reported in the literature for determining this texture feature. For this purpose, this paper presents a suitable local texture criterion to determine it. A comprehensive evaluation combining the local texture features and a modified shape criterion is proposed to improve recognition capability. To increase the processing speed, a specifically designed target-searching strategy is also described, which reduces the time cost by avoiding the unnecessary labeling process for most nontarget regions and by calculating some key parameters in advance. To validate the efficiency of our proposed method, a prototype for a handheld detecting system was built for laboratory experiments.

This paper is organized as follows: Sec. 2 introduces the principles of the cat's eye effect, the qualities of interior environments, the modified shape criterion, and the local texture criterion. Section 3 introduces the target candidate searching strategy and the proposed evaluation method. Section 4 describes the technical specifications of the prototype and the laboratory experiments. The results and discussion are in Sec. 5. Section 6 presents the conclusions.

*Address all correspondence to: Bao Zhang, E-mail: zhangb@ciomp.ac.cn

0091-3286/2015/$25.00

2 Principles

2.1 *Retroreflection*

A retroreflection signal can be obtained from the target optical system (TOS), which can act as a retroreflector. The reflected rays and radiant energy of a retroreflector are parallel to the incident rays at any angle of incidence within the field of view (FOV).[5] The retroreflector can be a corner cube or an optical system consisting of at least a focusing lens and a surface with some degree of reflectivity. Examples of TOSs include cameras, telescopes, sight scopes, and animal/human eyes. This retroreflecting quality is also called the cat's eye effect. One fundamental feature of the retroreflector is that the retroreflection is higher than the diffuse background scattering by 2 to 4 orders of magnitude.[5,6,12,13] "Background" here indicates the targets with average surface characteristics, where "average" refers to the nature of the target surface, i.e., without any special surface preparation or polishing.[14]

2.2 *Characteristics Analysis*

Generally, interior optical device counter-surveillance applications are utilized at short-operating distances and static backgrounds. The passive image [Fig. 1(b)] can be directly subtracted from its active counterpart [Fig. 1(a)] without further registration because of the static background. However, in interior environments, there are surfaces with high reflectivity, such as painted furniture, specular objects, and polished metal, generating glints. Glints may be as strong as the retroreflection assigned to a retroreflector owing to the short operating distance. These glints are typical examples of false positives. Consequently, interior environments present more challenges than open terrain. In the interior scenario (Fig. 1), false alarms are mainly caused by high-reflecting clutter, which may exhibit similar reflection to that of the targets. In typical field scenes, the targets are usually solitary with fewer false alarms; furthermore, the interference is mainly from the dynamic background. Urban scenes are heterogeneous and may contain several different false targets. Method reported in the literature examines urban scenes by incorporating different devices that capture other features of the optical systems. However, these devices are either very expensive or unsuitable for interior applications owing to their principles, weights, volumes, or processing speeds.

The optical retroreflector has two distinctive features: the target retroreflection is brighter than that of most objects and, in most cases, its shape is almost circular owing to the shape of the optical cross sections. These features have been widely investigated in the literature. Actually, the subtraction image in the interior environment [Fig. 1(c)] provides extensive texture information. However, this feature has not been fully utilized; in contrast, it is discarded in the process of

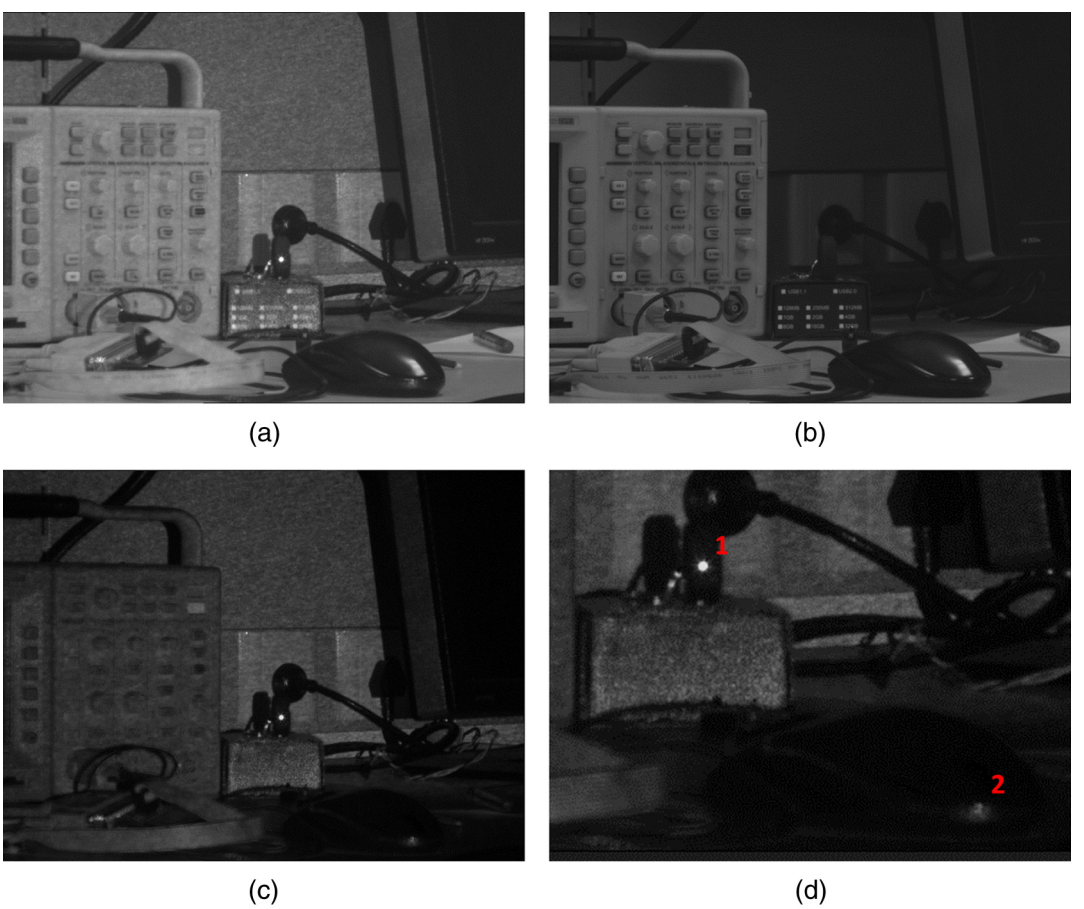

Fig. 1 The principle of detection in the interior scenario: (a) the active image is subtracted from (b) the passive image; (c) the subtraction image; and (d) two reflecting spots representing retroreflection and dispersed reflection.

generating binary images either by thresholds or gated sensors (e.g., Silicon ICCD[5]). The retroreflection spot appears as a local maximum, e.g., it generally has a "top-hat" distribution shape with a sharper edge than that of the spot originating from a dispersed reflecting surface (Fig. 2). In contrast, the texture of disturbing objects has some degree of continuity with that of the surroundings, as shown in Fig. 2(b). Accordingly, it is appropriate to adopt the contrast between the TOS and its surroundings as the texture criterion. A local texture criterion is therefore proposed, which is based on the assumption that the TOS has a sharper contrast to its surroundings (local maximum) than the false positives while the surroundings exhibit less continuity. The mathematical description of the local texture feature will be discussed in Sec. 2.4.

2.3 *Modified Shape Criterion*

The retroreflected spots of optical threats are almost circular. Therefore, the shape criterion has been widely considered as the first stage of false alarm reduction—spots with parametric values larger than a certain threshold are discarded. There are four versions of the shape criterion, as shown in Table 1, including roundness, circularity, eccentric distance, and eccentric ratio.

The performance of the four criteria relies on the number of occupied discrete samples and the random quantization errors of the binary image. The major and minor axes are vulnerable to quantization errors. The roundness is less error-sensitive than the eccentric distance/ratio and faster to calculate than the circularity but less accurate than the eccentricity. Accordingly, a modified comprehensive shape metric is proposed and defined as

$$M_c = |C_1 - 1| + P_1, \tag{1}$$

$$P_1 = \frac{|a-b|}{|a+b|}. \tag{2}$$

The ideal value of the comprehensive shape metric M_c is 0 when the shape is perfectly circular. A threshold of 0.9 was selected in the calculations. Spots with shape metric values below the threshold were regarded as circular.

Table 1 Shape criterion options.

Constraint	Expression	Parameters
Roundness	$C_1 = \frac{L^2}{4\pi S}$	L, perimeter; S, area
		$\mu = \frac{1}{L}\sum_{l=0}^{L} \|(x_l, y_l) - (\bar{x}, \bar{y})\|$: average distance
Circularity	$C_2 = \frac{\mu^2}{\sigma}$	$\sigma = \frac{1}{L}\sum_{l=0}^{L} \|(x_l, y_l) - (\bar{x}, \bar{y}) - \mu\|$: mean square deviation
		$\bar{x} = \frac{1}{L}\sum_{(x,y)\in R} x$; $\bar{y} = \frac{1}{L}\sum_{(x,y)\in R} y$: barycenter
Eccentric distance	$P_d = \|a - b\|$	a, major axis; b, minor axis
Eccentric ratio	$P_r = \frac{a}{b}$	a, major axis; b, minor axis

2.4 *Proposed Local Texture Criterion*

The proposed texture criterion is derived from the RX algorithm,[15] which is used for anomaly detection in multi and hyperspectral imagery. The criterion determines the contrast of a target region with its surroundings. The proposed texture criterion for a singular pixel, denoted as $\delta_{TC}(x, y)$, is

$$\delta_{TC}(x, y) = [I_t(x, y) - \mu_b]^2, \qquad (x, y) \in \mathbf{R}_t \tag{3}$$

or

$$\delta_{TC}(x, y) = |I_t(x, y) - \mu_b|, \qquad (x, y) \in \mathbf{R}_t, \tag{4}$$

where $I_t(x, y)$ denotes the gray level of a single pixel belonging to the set $\mathbf{R}_t$. $\mathbf{R}_t$ represents the target region in the subtraction image (see Fig. 3). The set $\mathbf{R}_t$ corresponds to the set of the target spot in the binary image. μ_b is a statistical parameter of the surroundings of the target spot and is described as

$$\mu_b = \frac{1}{card\,\mathbf{R}_b} \sum_{(x,y)\in\mathbf{R}_b} [I_b(x, y) - \bar{I}_b(x, y)]^2 \tag{5}$$

or

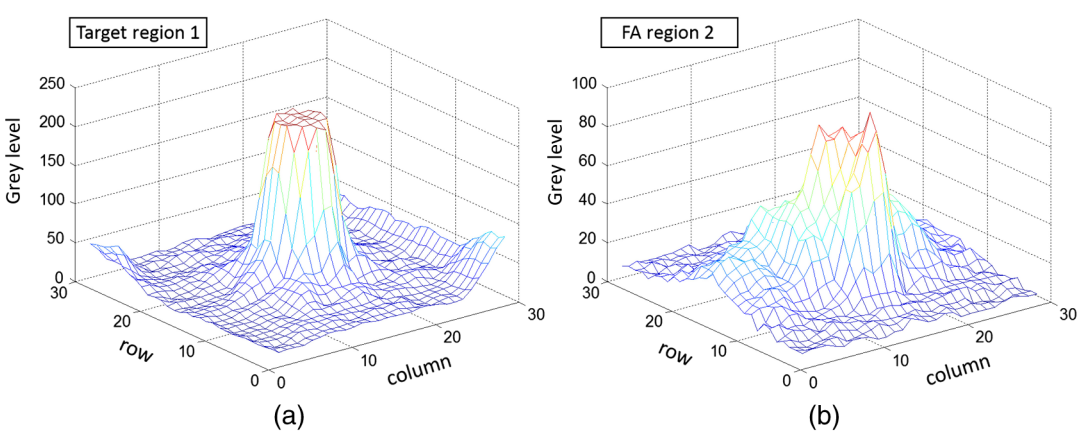

Fig. 2 The distribution of the two labeled spots in Fig. 1(c): (a) retroreflection and (b) dispersed reflection.

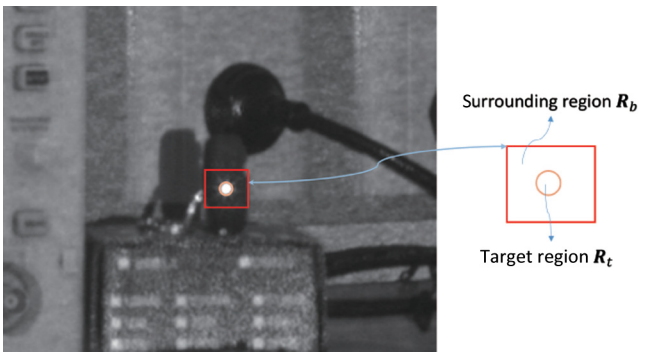

Fig. 3 The target region and its surrounding region.

$$\mu_b = \frac{1}{card\,\mathbf{R}_b} \sum_{(x,y)\in\mathbf{R}_b} |I_b(x,y) - \bar{I}_b(x,y)|. \tag{6}$$

$I_b(x,y)$ is the gray level of the pixels in the surrounding region, and $\bar{I}_b(x,y)$ is the corresponding mean value. $\mathbf{R}_b$ is the set of the surrounding region, and $card*$ denotes the number of all the elements in a set. The size of $\mathbf{R}_b$ was selected to have sides 10 pixels longer than those of the smallest box containing the target region $\mathbf{R}_t$.

The mean value $\bar{\delta}_{\mathrm{TC}}(x,y)$ of the target region is

$$\bar{\delta}_{\mathrm{TC}} = \frac{1}{card\,\mathbf{R}_t} \sum_{(x,y)\in\mathbf{R}_t} \delta_{\mathrm{TC}}(x,y), \tag{7}$$

and the normalized standard deviation of the gray levels of the target region is

$$\sigma_T = \frac{1}{255}\sqrt{\frac{1}{card\,\mathbf{R}_t} \sum_{(x,y)\in\mathbf{R}_t} [I_t(x,y) - \bar{I}_t(x,y)]^2}, \tag{8}$$

where $\bar{I}_t(x,y)$ is the mean value of $I_t(x,y)$. We considered 255 as the normalization factor for the 8-bit image. The texture criterion for the spot is defined as

$$\dot{\delta}_{\mathrm{TC}} = \frac{\bar{\delta}_{\mathrm{TC}}}{\sigma_T + 1}. \tag{9}$$

As mentioned in Sec. 2.2, the retroreflector has a stronger retroreflected signal. Accordingly, the contrast of the mean gray levels between the target region and the background region is a feature that can distinguish them. μ_b reflects the statistical property of the continuity of the distribution of the surroundings. $\dot{\delta}_{\mathrm{TC}}$ expresses how distinct the target is from its surroundings. True retroreflecting objects typically have $\dot{\delta}_{\mathrm{TC}}$ values higher than 17, whereas false alarms have lower values.

3 System Scheme

A system consisting of a laser flood illuminating[16] the FOV and a CCD camera capturing retroreflection was developed. The laser illuminates every second frame to obtain the active and passive images. The nonilluminated passive image is then subtracted from the illuminated active image to suppress the background clutter. The subtraction image is used to generate the binary image. The binary image is utilized in the target candidate searching part and then the shape criterion is applied for coarsely reducing false alarms. The subtraction image is also used to reduce false alarms with the proposed local texture criterion.

The algorithm of our system consisted of three main stages (Fig. 4): preprocessing, TOS candidate searching, and target verification. In the preprocessing stage, the subtraction image was generated from the active and passive images. The binary image (Fig. 5), denoted as I_{bw}, had been filtered beforehand to eliminate noises. In the second stage, we applied a searching strategy incorporating the shape criterion to locate disjoint regions. Most unsuitable regions were excluded by using the shape criterion $|C_1 - 1|$. The surviving regions were recorded as the target candidates. In the verification stage, we calculated the texture criterion $\dot{\delta}_{\mathrm{TC}}$ of each target candidate using the subtraction image. Finally, a comprehensive evaluation combining the shape metric M_c and the proposed local texture criterion $\dot{\delta}_{\mathrm{TC}}$ was used to distinguish the true TOSs from false positives.

3.1 *Target Candidate Searching*

This study is aimed at finding hidden miniature optical devices within a relatively large FOV. The number of pixels that the optical cross section of the target occupies on a CCD/CMOS sensor array is usually smaller than 100. Retroreflection appears as a solid spot on the sensor array when the detecting camera is in focus. A mathematical morphology method was employed for the representation and description of region shapes. We designed two concentric

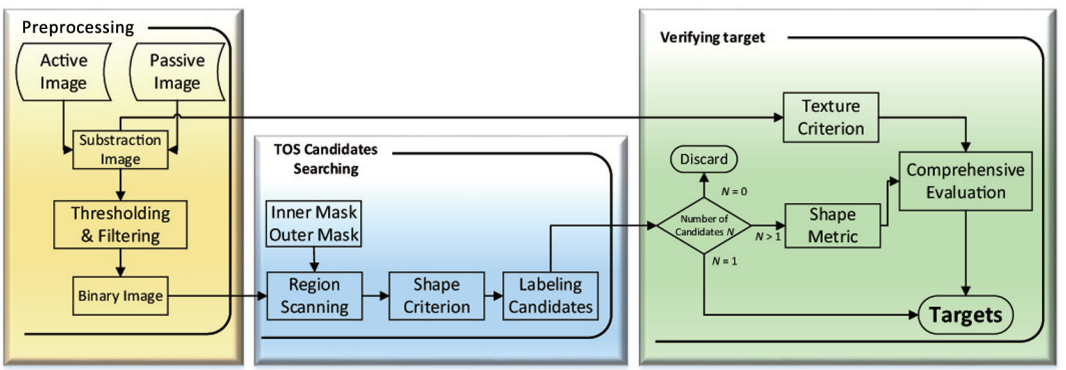

Fig. 4 Flowchart of the proposed method.

Fig. 5 The binary image generated from Fig. 1(c).

masks (Fig. 6), an inner mask [Fig. 6(a)] and its outer counterpart [Fig. 6(b)], to perform morphological filtering by sliding across the binary image I_{bw} in one-pixel steps.

In matrix form, these two masks are described as

$$w_{\text{inner}} = \begin{bmatrix} 1 & 1 & 1 \\ 1 & 1 & 1 \\ 1 & 1 & 1 \end{bmatrix}_{3\times 3};$$

$$w_{\text{outer}} = \begin{bmatrix} 1 & 1 & \dots & 1 & 1 \\ 1 & 0 & \dots & 0 & 1 \\ \vdots & \vdots & \ddots & \vdots & \vdots \\ 1 & 0 & \dots & 0 & 1 \\ 1 & 1 & \dots & 1 & 1 \end{bmatrix}_{13\times 13}, \tag{10}$$

where w_{inner}, w_{outer}, and I_{bw} are the sets in $\mathbb{Z}^2$. The translation of set $A \in \mathbb{Z}^2$ by point $z = (z_1, z_2)$, denoted as $(A)_z$, is defined as

$$(A)_z = \{c | c = a + z, \text{for } a \in A\}. \tag{11}$$

The logic operation $\ominus$ of I_{bw} by w_{inner}, denoted as $I_{bw} \ominus w_{\text{inner}}$, is defined as

$$I_{bw} \ominus w_{\text{inner}} = \{z | (w_{\text{inner}})_z \subseteq I_{bw}\}, \tag{12}$$

and the logic operation $\circledcirc$ of I_{bw} by w_{outer}, denoted as $I_{bw} \circledcirc w_{\text{outer}}$, is defined as

$$I_{bw} \circledcirc w_{\text{outer}} = \{z | (w_{\text{outer}})_z \cap I_{bw} = \varnothing\}, \tag{13}$$

where $\varnothing$ denotes an empty set.

The 3×3 inner mask w_{inner} determines the solid disjoint regions using Eq. (12) and the 13×13 outer mask w_{outer} filters out the regions that exceed the mask borders using Eq. (13). The outer mask functions as an area constraint that limits the size of the reflection spot. By combining these two masks, all candidates within an area of 11×11 pixels and containing at least one solid 3×3 patch survive, like the example displayed in Fig. 6(c).

Let I_{index} be a set in $\mathbb{Z}^2$, which is used to record the potential centroids of the surviving target candidate regions. This is formulated as

$$I_{\text{index}} = (I_{bw} \ominus w_{\text{inner}}) \cap (I_{bw} \circledcirc w_{\text{outer}}). \tag{14}$$

A target candidate region may contain more than one potential centroids, as shown in Fig. 6(d) (which includes five potential centroids). Therefore, the rounded mean of these potential centroids for each region is used as the index of these target candidate regions. Let a series of subsets $\{R(\xi) | R(\xi) \subseteq I_{bw}, \xi \in \mathbb{N}\}$ denotes all the disjoint regions in I_{bw}. The index of the target candidate region, denoted as $\hat{I}_{\text{index}}$, is

$$\hat{I}_{\text{index}} = \{\bar{z} | z \in [R(\xi) \cap I_{\text{index}}], \xi \in \mathbb{N}\}, \tag{15}$$

where $\bar{z}$ represents the mean value of z.

In conventional methods, all the disjoint regions of various shapes and sizes are located and labeled at the very first ergodic searching stage. Then the area or shape of a certain region is considered as a constraint. However, most of the labeled regions are excluded in the subsequent processes; therefore, labeling numerous discarded regions is ineffectual. In our searching scheme, the area constraint is merged with the ergodic searching step by using the outer mask, which avoids the clustering and labeling process of the subsequently discarded regions. The infinitesimal or air-core regions are excluded by using the inner mask. Therefore,

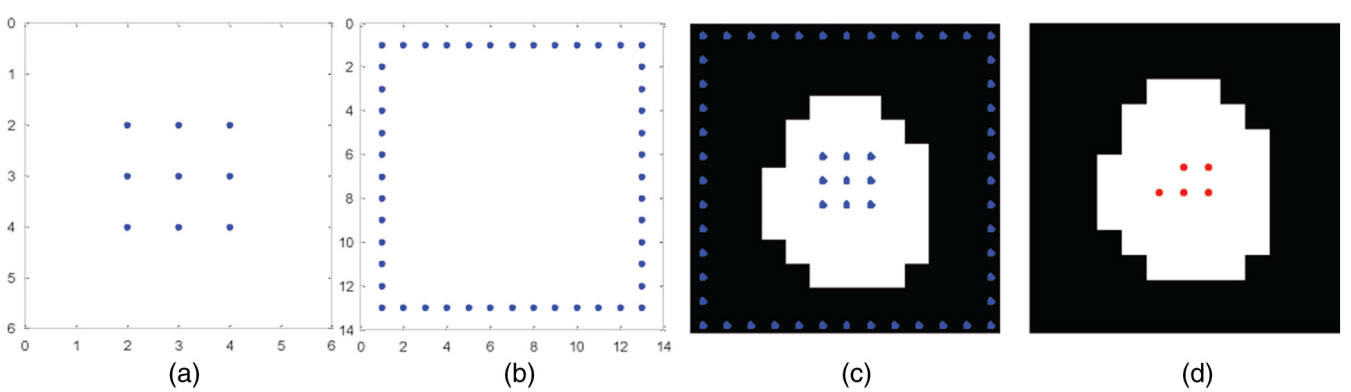

Fig. 6 The principle of target candidate searching: (a) The inner and (b) outer masks, used separately for the morphological filtering; (c) example of surviving candidates; and (d) several potential centroids of the example candidate.

the shape of the target region is partly controlled by using the dual masks. This dual-mask-filtering searching method outperforms the conventional approaches when the target regions are below a certain size, especially when the background contains numerous false alarms of various shapes and sizes.

3.2 *False Alarm Reduction*

This task aims to determine whether a target candidate region ξ is a true TOS or a false positive. It is typically formulated as a binary hypothesis test:

$$\mathcal{H}(\xi) = \begin{cases} H_0: \text{region } \xi \text{ is a false positive;} \\ H_1: \text{region } \xi \text{ is a target optical system.} \end{cases} \tag{16}$$

The false-alarm reduction process is divided into two parts: the application of the shape criterion in stage 2 and a comprehensive evaluation in stage 3 (Fig. 4). The first part considers $|C_1 - 1|$ as the shape criterion. It eliminates most unsuitable regions that have a shape far from circular or a size larger than the threshold. If only one target candidate region survives the first part, then this region is regarded as the TOS without proceeding to the second part (the comprehensive evaluation). When two or more target candidates survive, the comprehensive evaluation is performed. The $\dot{\delta}_{\mathrm{TC}}$ value for each target candidate is calculated based on the subtraction image. Finally, the comprehensive evaluation combining the shape metric and the local texture criterion is utilized, which is defined as

$$\Psi(\xi) = \frac{\dot{\delta}_{\mathrm{TC}}(\xi)}{M_{\mathrm{c}}(\xi)} \underset{H_0}{\overset{H_1}{\gtrless}} \eta. \tag{17}$$

η is an empirical detection threshold. The target candidate ξ with the highest value of Ψ has the highest probability to be the true TOS.

4 Experimental Setup

We constructed a prototype of the detecting system consisting of a video camera and a laser illuminator. The key specifications are shown in Tables 2 and 3.

The typical gray levels of background clutter varied below 50. The video camera was directly connected to a plug-in image grabber installed in a desktop computer. All the programs were developed in C language and tested on the VC2010 platform with Intel Core i3-2120 CPU. We selected four different miniature cameras with aperture diameters of 1 to 2 mm as the experimental targets. Several high-reflectivity metal objects were selected as the interference (Fig. 7).

Table 2 The key specifications of the camera.

Parameter	Characteristics
CCD	752(H) × 582(V) pixels
Lens	50-mm fixed focus; $F^{\sharp}$14
Auto gain control	Off
FOV	10 deg

Table 3 The key specification of the laser illuminator.

Parameter	Characteristics
Wavelength	808 nm
Power	1 W
Divergence angle	30 deg
Control mode	Voltage
Beam profile	Round; Gaussian

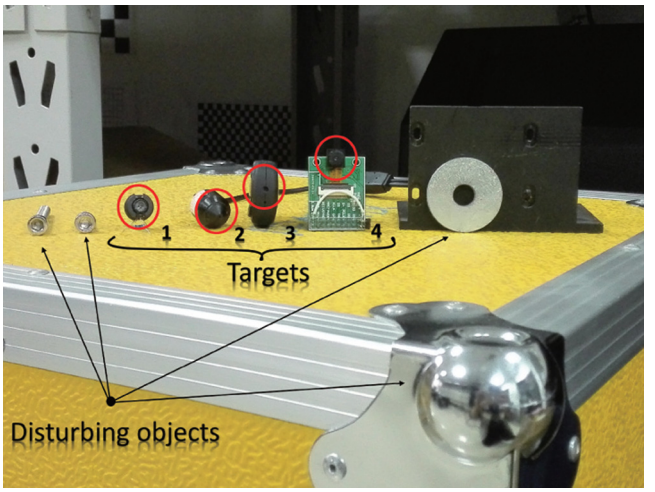

Fig. 7 The experimental targets (middle) and disturbing objects.

Experiments were performed under different complex backgrounds with interference to evaluate the practicability of our proposed method. The experimental scenes included metal surfaces and edges or other clutter with high reflectivity. Some experimental scenes contained disturbing objects with similar reflection spot shapes to those of the true TOSs. The operating distances from the detecting system to the experimental targets were set at 2.2, 3.2, and 4.2 m. At each operating distance, the prototype was tested repeatedly; and 100 results were recorded for statistics.

5 Results and Discussion

Figure 8 shows one of these experiments, performed at the distance of 2.2 m. An empirical threshold $|C_1 - 1|_{\mathrm{TH}} = 0.4$ was employed in the target candidate searching step to coarsely eliminate the regions that were far from circular, resulting in 14 target candidates, which are labeled in Fig. 8(b). The related criteria and the comprehensive evaluation of the 14 regions are shown in Table 4. In the table, a higher value of $\dot{\delta}_{\mathrm{TC}}$ or Ψ indicates a higher probability for the region to be the target according to each criterion. For the other $|C_1 - 1|$ values, P_1 and M_{c}, a value near 0 indicates that the shape of the region is closer to circular. The bold values correspond to the experimental targets and the values in italics indicate a false alarm that could not be excluded by a certain criterion. For example, the M_{c} value of region 6 was larger than the smallest value, 0.5714 (region 3), of the four targets. Therefore, region 6 cannot be excluded by independently using the shape metric.

As seen in Table 4, the proposed evaluation Ψ excluded two false alarms that survived the modified shape criterion M_c and one false alarm that survived the local texture criterion $\dot{\delta}_{TC}$. However, one false alarm (region 1) remained, which originated from the high-reflecting spherical surface shown in Fig. 8(b). Figure 9 illustrates the distribution of the eight regions with the highest evaluation values Ψ; four experimental targets are displayed in the first row and four false alarms are in the second row. As shown in Fig. 9(e), the false alarm region 1 had similar distribution features to those of a true TOS. Thus, it could not be discriminated according to the features summarized in Sec. 2.2.

Table 4 also indicates that the modified shape criterion M_c showed improved shape measurement accuracy than the conventional shape criterion, as demonstrated by the comparison of Table 4 with Fig. 9. The proposed evaluation outperformed both the conventional shape criterion and its modified version by accurately measuring the shape and texture features of the distribution and by excluding other metal objects with high reflectivity, e.g., regions 6 and 11; this was because these metal objects had some degree of continuity, which was reflected in the distribution [see Figs. 9(f)–9(h)]. Consequently, these two regions can be discriminated by the proposed texture criterion $\dot{\delta}_{TC}$ and excluded by the comprehensive evaluation Ψ.

To verify the superiority of our dual criteria method, a comparison of the recognition capabilities of the shape criterion M_c, the texture criterion $\dot{\delta}_{TC}$, and the evaluation Ψ for experimental scene 1 with varying operating distances is

Table 4 Criterion evaluation of experiment 1.

Region	Centroid	$\lvert C_1 - 1\rvert$	P_1	M_c	$\dot{\delta}_{TC}$	Ψ
1	[145,456]	0.2261	0.5276	*0.7428*	*19.46*	*26.20*
2	[185,606]	0.0286	0.9675	0.9961	16.44	16.50
3	[211,253]	0.2857	0.2857	**0.5714**	**19.07**	**33.37**
4	[212,178]	0.2895	0.5830	**0.8725**	**18.80**	**21.55**
5	[223,526]	0.1860	0.8073	0.9933	16.26	16.36
6	[224,657]	0.3446	0.5139	*0.8585*	*17.83*	20.76
7	[226,331]	0.3277	0.4635	**0.7912**	**17.74**	**22.41**
8	[242,648]	0.2744	0.6265	0.9009	16.91	18.78
9	[243,519]	0.1182	0.8692	0.9873	16.08	16.29
10	[275,422]	0.2994	0.4675	**0.7669**	**18.77**	**24.48**
11	[295,525]	0.0004	0.8011	*0.8014*	14.95	18.65
12	[297,658]	0.1429	0.9149	1.0577	11.37	10.75
13	[311,648]	0.1995	0.9856	1.1851	12.62	10.65
14	[315,520]	0.2161	0.8654	1.0815	15.95	14.75

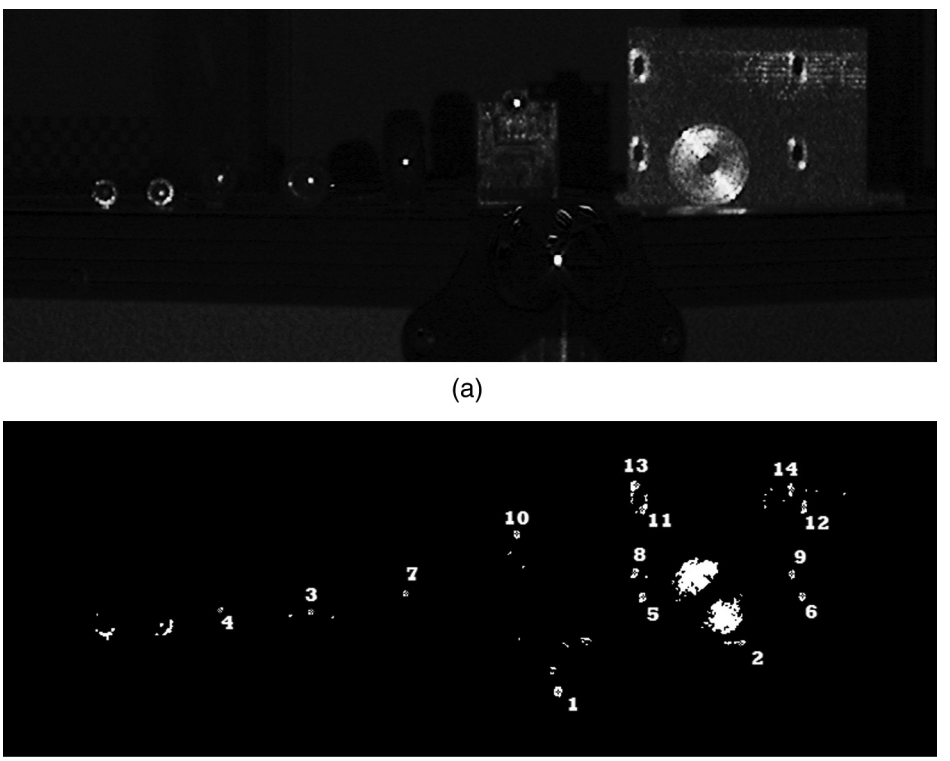

(a)

(b)

Fig. 8 One of the experimental scenes at the distance of 2.2 m: (a) the subtraction image; and (b) the resulting binary image after the target-searching stage with 14 labeled surviving candidates.

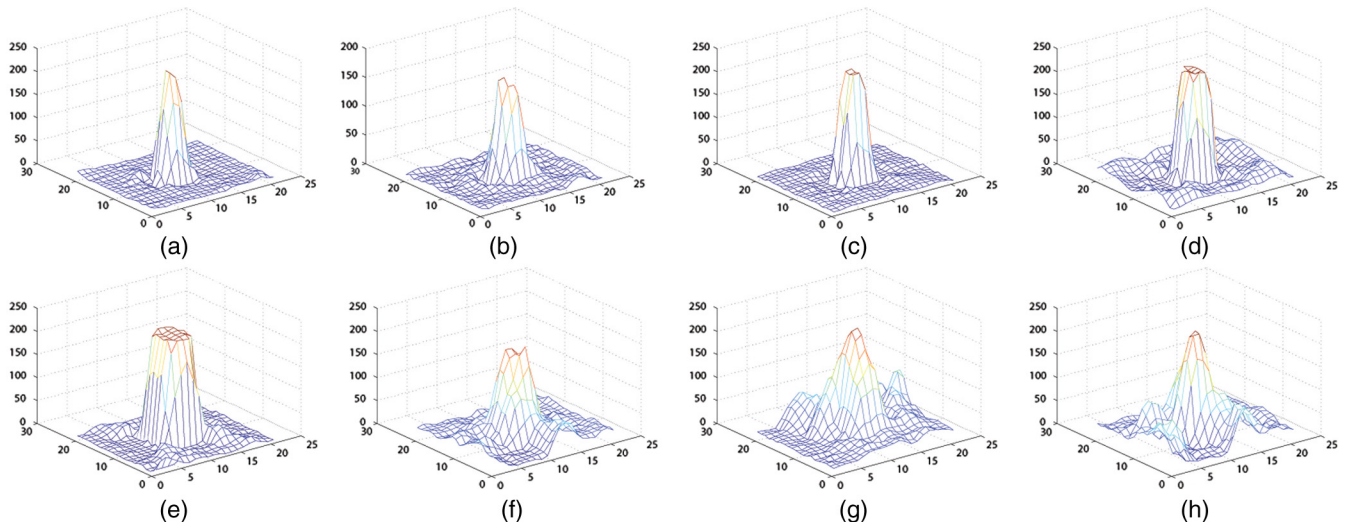

Fig. 9 The distribution of the true targets and the false alarm regions: (a)–(d) the true targets, labeled as 3, 4, 7, and 10 in Fig. 8(b); and (e)–(h) the false alarm regions, labeled as 1, 6, 8, and 11 in Fig. 8(b).

Table 5 The recognition probabilities for experimental scene 1.

Target	2.2 m			3.2 m			4.2 m		
	M_c (%)	$\dot{\delta}_{TC}$ (%)	Ψ (%)	M_c (%)	$\dot{\delta}_{TC}$ (%)	Ψ (%)	M_c (%)	$\dot{\delta}_{TC}$ (%)	Ψ (%)
1	23	38	49	17	42	54	39	62	73
2	31	25	43	46	46	62	50	51	65
3	58	42	66	53	50	62	72	62	78
4	62	87	92	75	83	85	56	50	67

shown in Table 5 and Fig. 10. According to the table, the recognition probability of the proposed method is higher than that of the other two methods. Additionally, as Fig. 10 shows, there is no obvious correlation between the recognition probability and the operating distance; this is because within a certain range, the operating distance was not a main influencing factor. The main influencing factor was the presence of disturbing objects with polished spherical metal surfaces or circular objects with high reflectivity in the background. The features of the distribution responding to those objects and their local surroundings were similar to those of the targets. Accordingly, the comprehensive evaluation of the targets exhibits no superiority over the other two criteria. As shown in Figs. 9(a)–9(d), target regions 3 and 4 have some degree of asymmetric aberrance and regions 7 and 10 generated a higher response than regions 3 and 4. This was due to the incidence angle of the laser beam, which is another influencing factor.[12,17]

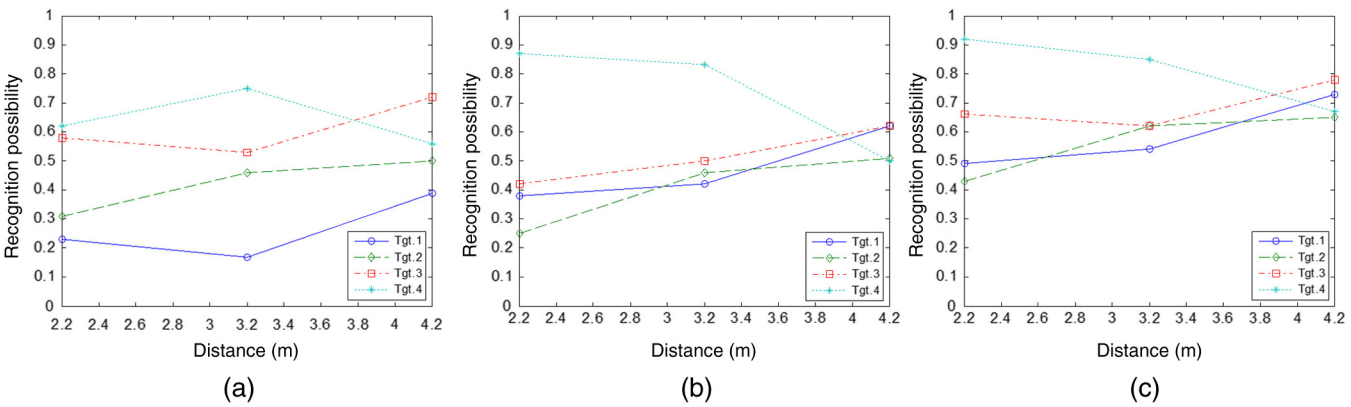

Fig. 10 Variations of recognition probability with distance and method: (a) results of the shape criterion M_c; (b) results of texture criterion $\dot{\delta}_{TC}$; and (c) results of evaluation Ψ.

Table 6 The results for the other experimental scenes (without spherical surfaces).

Target	Experimental scene 2			Experimental scene 3			Experimental scene 4		
	M_c (%)	$\dot{\delta}_{TC}$ (%)	Ψ (%)	M_c (%)	$\dot{\delta}_{TC}$ (%)	Ψ (%)	M_c (%)	$\dot{\delta}_{TC}$ (%)	Ψ (%)
1	48	62	84	41	65	82	62	78	94
2	55	51	81	68	68	88	70	71	91
3	76	65	93	73	71	95	85	62	95
4	79	87	97	87	91	98	75	71	96

To extend the verification to the other experiments, three other experimental scenes were investigated with operating distances of 2.2, 3.2, and 4.2 m and without spherical metal surfaces (Fig. 8). The overall result of the recognition probability, neglecting distance variations, is shown in Table 6. As seen in the table, the proposed evaluation Ψ is much superior over the other two methods in recognition probability.

In summary, the recognition probability was not consistently high in all our experiments. That was because the false positives caused by the spherical reflecting surfaces could not be eliminated owing to their reflecting characteristics and the short measurement distances. In other cases, when circular objects with strong reflectivity were present in the background, the recognition rates decreased. However, the proposed evaluation method determined the texture feature of the target regions more accurately and performed much better than the conventional shape criterion in eliminating high-reflectivity objects with some degree of continuity reflected in the distribution.

In addition, the average time cost of the entire detection and recognition process was 0.0804 s. This can be further improved by optimization of the codes and hardware. As reported in Ref. 18, the shape-frequency dual criteria (SFDC)[2] method has an average running time of 6.182 s, the method that uses sample processing before reconstruction based on compressed sensing (SPCS)[3] requires about 3.435 s, and the multichannel saliency processing before fusion (MSPF)[18] method needs 1.852 s in parallel mode and 1.203 s in serial mode. The testing CPU reported in Ref. 18 was the Pentium Dual-Core CPU, which is based on the same architecture with the one we used. Thus, we considered the performances of the two CPUs are comparable. However, the running time of our method is 6.68% of the shortest time of the reference methods. Therefore, our method exhibited a superior average processing speed, which is a very significant advantage for handset devices. This enhances the quality of the detecting device, which can acquire and process multiple images by the repetitive detection and recognition of nearly the same scene (in a slow-scanning scheme). Thus, the recognition probability is also improved.

6 Conclusion

The results showed that the proposed method achieved improved recognition probability. The modified shape criterion measured the distribution shape more accurately and the local texture criterion successfully reflected the local maximum of the target and the continuity between the target and its surroundings. The disjoint region searching strategy, combined with some shape constraints, reduced the processing time by avoiding the unnecessary labeling process for most nontarget regions and by calculating some key parameters used in the subsequent procedures. The presented method also showed superior processing speed to the SFDC, SPCS, and MSPF methods. In addition, it does not require high costs for extra detectors and complex mechanisms and it is beneficial for the development of real-time counter-surveillance devices for preventing information leaks.

Our future studies will focus on exploiting other features to eliminate false alarms which caused by high-reflectivity spherical or circular surfaces with a comparable size with the lens of a miniature camera.

Acknowledgments

This study was supported partly by the Major Innovation Program of Changchun Institute of Optics, Fine Mechanics and Physics, Chinese Academy of Sciences (Grant No. y3cx1ss14c) and the Programs Foundation of Key Laboratory of Airborne Optical Imaging and Measurement, Chinese Academy of Sciences (Grant No. y3hc1sr141).

References

1. C. Lecocq et al., "Sight laser detection modeling," *Proc. SPIE* **5086**, 280–286 (2003).
2. X. Ren and L. Li, "Recognizing cat-eye targets with dual criterions of shape and modulation frequency," *Chin. Opt. Lett.* **9**(4), 42–45 (2011).
3. L. Li et al., "Compressive sensing method for recognizing cat-eye effect targets," *Appl. Opt.* **52**, 7033–7039 (2013).
4. L. Sadler and T. A. Alexander, "Mobile optical detection system for counter-surveillance," *Proc. SPIE* **7694**, 76940Y (2010).
5. M. Auclair, Y. Sheng, and J. Fortin, "Identification of targeting optical systems by multiwavelength retroreflection," *Opt. Eng.* **52**(5), 054301 (2013).
6. L. Sjöqvist et al., "Optics detection using a dual channel approach," *Proc. SPIE* **8543**, 85430F (2012).
7. G. S. Buller and A. M. Wallace, "Ranging and three-dimensional imaging using time-correlated single-photon counting and point-by-point acquisition," *IEEE J. Sel. Top. Quantum Electron.* **13**, 1006–1015 (2007).
8. M. Henriksson and L. Sjöqvist, "Time-correlated single-photon counting laser radar in turbulence," *Proc. SPIE* **8187**, 81870N (2011).
9. M. V. Scanlon and W. D. Ludwig, "Sensor and information fusion for improved hostile fire situational awareness," *Proc. SPIE* **7693**, 76930H (2010).
10. D. Lindgren et al., "Multisensor configurations for early sniper detection," *Proc. SPIE* **8186**, 81860D (2011).
11. G. Mooradian et al., "System and method for detecting a camera," U.S. Patent No. 8,184,175,B2 (2012).
12. Y. Zhao, H. Sun, and Y. Zheng, "An approximate analytical propagation formula for Gaussian beams through a cat-eye optical lens under large incidence angle condition," *Chin. Phys. Lett.* **28**(7), 074101 (2011).
13. Z. Hou, Y. Li, and S. Wang, "The research of cat-eye target laser active detection system performance," *Proc. SPIE* **9142**, 914224 (2014).
14. N. J. Abel et al., "Wave-optics modeling of aberration effects in optical cross section measurements," *Opt. Eng.* **44**(8), 084302 (2005).

15. I. Reed and X. Yu, "Adaptive multiple-band CFAR detection of an optical-pattern with unknown spectral distribution," *IEEE Trans. Acoust., Speech, Signal Process.* **38**, 1760–1770 (1990).
16. L. Sjöqvist et al., "Target discrimination strategies in optics detection," *Proc. SPIE* **8898**, 88980K (2013).
17. Y. Zhao et al., "Three-dimensional analytical formula for oblique and off-axis Gaussian beams propagating through a cat-eye optical lens," *Chin. Phys. Lett.* **27**(3), 034101 (2010).
18. L. Li, J. Ren, and X. Wang, "Fast cat-eye effect target recognition based on saliency extraction," *Opt. Commun.* **350**, 33–39 (2015).

Feng Qain is a doctoral candidate at the University of the Chinese Academy of Sciences. He received his BS degree in electronic technology and information science from the University of Science and Technology of China in 2011. His PhD research is at the Changchun Institute of Optics, Fine Mechanics and Physics, Chinese Academy of Sciences. His current research interests include electro-optical system software design, image processing and analysis, and pattern recognition.

Bao Zhang is a professor at the University of the Chinese Academy of Sciences. He is also the director of the Department of Airborne Optical Imaging and Measurement, Changchun Institute of Optics, Fine Mechanics and Physics, Chinese Academy of Sciences. He is the author of more than 80 journal papers and has written several book chapters. His current research interests include electro-optical system design and analysis, remote sensing signal, and data processing.

Biographies for the other authors are not available.